Separation and Purification Technology 353 (2025) 128599

Contents lists available at ScienceDirect

Separation and Purification Technology

journal homepage: www.elsevier.com/locate/seppur

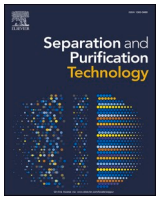

Recovery of rare earth elements from mining wastewater with aminomethylphosphonic acid functionalized 3D-printed filters

Emilia J. Virtanen [a,c], Esa Kukkonen [a,c], Janne Yliharju [b,c,d], Minnea Tuomisto [e], Janne Frimodig [a], Kimmo Kinnunen [b,c], Elmeri Lahtinen [a,1], Mikko M. Hänninen [a,1], Ari Väisänen [a], Matti Haukka [a], Jani O. Moilanen [a,c,*]

[a] Department of Chemistry, University of Jyväskylä, P.O. Box 35, FI-40014 Jyväskylä, Finland
[b] Department of Physics, University of Jyväskylä, P.O. Box 35, FI-40014 Jyväskylä, Finland
[c] Nanoscience Center, University of Jyväskylä, P.O. Box 35, FI-40014 Jyväskylä, Finland
[d] School of Resource Wisdom, University of Jyväskylä, P.O. Box 35, FI-40014 Jyväskylä, Finland
[e] Department of Chemistry, University of Turku, FI-20014 Turku, Finland

ARTICLE INFO

Editor: Kuo-Lun Tung

Keywords:
Rare earth elements
3D printing
Mining waste
Recovery
Separation

ABSTRACT

Herein we report the use of nylon-12-based 3D-printed filters incorporating α-aminomethylphosphonic acid as an active additive for the recovery of Y, Nd, and Dy from the mining waste solution containing Al, K, Ca, Sc, Fe, Co, Cu, Zn, Y, Nd, Dy, and U. Nylon-12 was chosen for the polymer matrix of the filter due to its inactivity towards the studied metals. The micrometer-level structure of the filters was studied with a scanning helium ion microscope and X-ray tomography to reveal the porosity, pore size, and active additive distribution in the filters. Furthermore, FTIR spectroscopy was used to analyze the compositional changes in the 3D-printed filters after the printing and adsorption processes. Adsorption of the metals was studied at a pH range of 1–4, and the following adsorption trend Sc > Fe > U > Y, Nd, Dy > Al, Cu, Zn > K, Ca, Co was observed in each of the studied pH values. The sequential recovery process for metals was studied at pH 2, and desorption of the metals from the filters was performed with 6 M HNO_3. 100 % adsorption of REEs, Fe, and U was achieved during the recovery process, and on average, over 88 % of the adsorbed Y, Nd, and Dy were desorbed from the filters. In contrast to Y, Nd, and Dy, the desorption of Sc, Fe, and U was minimal (Fe and U) or negligible (Sc) with 6 M HNO_3 due to their strong coordination to the active additive. Maximum adsorption capacities for Y, Nd, Dy, and U were determined by using linear Langmuir adsorption isotherm. The best maximum adsorption capacity was determined for Sc, Q_{max} = 0.51 mmol/g followed by U, Nd, Dy, and Y with capacities of 0.47, 0.24, 0.23, and 0.17 mmol/g, respectively. Overall, this study achieved a complete removal of Sc, Fe, and U from the simulated mining waste solution leaving a final eluate that mainly contained Y (320 μg), Nd (350 μg), Dy (330 μg), and Al (710 μg) demonstrating the applicability of the 3D-printed filters in the recovery of Y, Nd, and Dy from the multimetal solution.

1. Introduction

Mining waste, which is a by-product of extracting and processing of mineral resources, is one of the largest waste streams in the European Union with roughly 500 megatons produced in 2020 [1]. Mining waste includes topsoil material, such as sedimentary rocks which are removed to access mineral resources, as well as waste rocks and tailings which are left behind after valuable metals are extracted from minerals [2,3]. It has been estimated that the annual production of tailings alone is up to 13 gigatons globally [4]. When sulphide-rich mineral waste is exposed to air and water, it oxidizes and forms sulfuric acid causing acid mine drainages (AMD). These drainages can be concentrated with metals, not only because of the sulphide ores but also due to the acid leaching of the surrounding minerals [5]. Depending on the types of minerals and the target metals in a main extraction process, the (metal) composition of the mining waste varies greatly. For example, mine tailings from Pb, Ag, and Zn mining activity in Mazarron, Spain, consist of high amounts of Al, Mn, Fe, Cu, Zn, As, Cd, and Pb along with elevated amounts of Ge,

* Corresponding author at: Department of Chemistry, Nanoscience Center University of Jyväskylä, P.O. Box 35, Jyväskylä FI-40014, Finland.
E-mail address: jani.o.moilanen@jyu.fi (J.O. Moilanen).
[1] Present address: Weeefiner Oy, 40530 Jyväskylä, Finland.

https://doi.org/10.1016/j.seppur.2024.128599
Received 20 March 2024; Received in revised form 16 June 2024; Accepted 26 June 2024
Available online 28 June 2024

Mo, Sn, Cs, La, Ce, Bi, Th, and U [6]. Out of these metals, Al, Mn, Ge, As, La, Ce, and Bi are classified as critical raw materials, for example, in the EU and US, due to their economic importance and supply risk [7,8]. Especially rare earth elements (REEs) are needed in a variety of modern technological applications and renewable energy production [9], whereas Al, Mn, and Bi are used in a variety of alloys. Tailings from quartzite and quarzitic sandstone mines in Kielce, Poland, consist of elevated amounts of As and REEs due to the AMD leaching the metal (loid)s from the surrounding minerals [10]. Valuable sources for REEs can additionally be found in the mining waste of apatite ores, phosphogypsum, from which up to 80 % of REEs can be leached out for further recovery processes [11,12]. Lixiviates from the Iberian Pyrite Belt could account for the production of 24 t/year of REEs, 34 t/year of Co, and 7000 t/year of Mg [13], all of which are classified as critical elements, whereas from Idaho Springs mine tailings up to 985 kg of REEs could be recovered annually [14].

The recovery of elements from mining waste typically includes a combination of hydrometallurgical processes such as leaching the target metals from the mining waste [15,16], precipitating the metals out from leachate or mine wastewater [17–19], and/or ion exchange [20,21] to separate the elements from other metals and impurities. In ion exchange, a solution containing metals is passed through a resin containing functional groups that selectively coordinate to one or more of the target metals [22]. Commercial ion exchange resins typically contain sulfonic, carboxylic, (amino)phosphonic, or iminodiacetic acids as functional groups that are capable of cation exchange [23]. Silica-based materials have also been studied for the recovery of REEs [24]. Aminophosphonates have shown great promise as chelating agents in ion-exchange resins due to their generally low toxicity [25–27], ability to coordinate with metals, such as Cu, Zr, REEs, Th, and U [28], and robustness in acidic conditions [29,30]. Virolainen *et al.* have studied REE extraction from phosphogypsum with aminophosphoric acid functionalized resin and obtained recovery rates up to 75 % for REEs. However, the reported purity of the REE fraction was 20 % due to the strong coadsorption of Ca [31]. Phosphonate functionalized mesoporous silica was found to be a selective adsorbent for U at pH 3, and U-containing solutions could be enriched up to 15-fold [32]. With the commercial aminophosphonate-functionalized resin TP260, REEs were completely extracted from the acidic solution even at a low pH value of 0.5, but Al coextracted completely with REEs [33]. Hermassi *et al.* have studied three commercial resins functionalized with sulfonic, aminophosphonic, and sulfonic/phosphonic groups for treating acidic mine waters containing Mg, Al, Ca, Mn, Fe, Co, Ni, Cu, Zn, Cd, and REEs. Although aminophosphonic-functionalized resin extracted over 90 % of the REEs present in the solution at pH 2, the best separation between the REEs and transition metals was achieved with the sulfonic resin [34]. Coextraction of Al, Fe Th, and U in conjunction with REEs has also been reported to occur with other commercial aminophosphonate resins [35,36].

3D-printed adsorption and ion exchange materials have increased their utilization in the solid phase extraction of metals because they are easy to manufacture, their sizes and shapes can be customized, and their active additives can be readily changed [37–39]. Thus, they can be adapted for a variety of different recovery and removal processes. For example, 90 % of U has been extracted from acidic media by 3D-printed material which has been coated with adsorbing quaternary ammonia resins [40], or 98 % from acidic solutions by a 3D-printed biopolymer filter with a solid/liquid ratio of 2 g/l [41]. 3D-printed devices have also been utilized for the preconcentration of Fe and Cr from low concentration-solutions enhancing the detection of these metals [42,43], and for removing radioactive ^{137}Cs and ^{90}Sr species from nuclear wastewater [44]. The selective recovery of Pd, Pt, and Au from waste electrical and electronic equipment (WEEE) by using the patented SLS 3D-printed filters has also been reported [45,46]. In these filters, the printing material consisted of either a functional polymer or hybrid material where a polymeric resin was used as the active additive. Another illustrative example was the selective removal of Cu from multimetal solutions using 3D-printed filters that were manufactured from a recycled polymer [38].

In the current work, we report a process for recovering Y, Nd, and Dy from a multimetal mining waste solution with the α-aminomethylphosphonic acid functionalized 3D-printed filters. The developed recovery process shows a reasonably good selectivity towards Y, Dy, and Nd among the investigated metals, while simultaneously minimize the amount of problematic coadsorbed metals, such as Al and Ca, in the final eluate. We demonstrate that 100 % of Fe, REEs, and U are adsorbed from the simulated mining waste solution with the 3D-printed filters in a low pH regime, and 88 % of adsorbed Y, Nd, and Dy can be desorbed, alongside some amount of Al, from the filters by acid elution. We also show that the 3D-printed filters are reusable in sequential adsorption–desorption cycles if the best adsorbing and accumulating metals, namely Sc, Fe, and U, are removed from the mining waste before the filtering process. Overall, the results demonstrate that the 3D-printed filters are robust and reusable for the recovery of critical rare earth metals from the multimetal mining waste solution.

2. Experimental

2.1. Materials and methods

Formaldehyde (36 %) was purchased from VWR, phosphorous acid (99 %) from Fluka Chemical Co., and dodecylamine (98 %) from Merck. All the chemicals were reagent grade and used without any further purification. 1000 mg/l standard solutions used for ICP-OES calibration of Al, K, Ca, Sc, Fe, Co, Cu, Zn, Y, Nd, Dy, and U in 5 % HNO_3 were purchased from Perkin Elmer. NMR measurements were performed on Bruker Avance III 300 MHz-spectrometer, and the obtained NMR data was processed with Bruker TopSpin 4.0.8. FTIR spectra were measured by Bruker Alpha FT-IR. Elemental analyses were conducted by Elementar Vario EL III- CHN analyser. Powder X-ray diffraction measurements were conducted with PANalytical Aeris. Flowrate for the adsorption/desorption experiments was controlled with Aladdin AL-1000 syringe pumps. Metal concentrations were determined by PerkinElmer ICP-OES Optima 8300 spectrometer. The filters were printed with ShareBot SnowWhite SLS 3D printer. X-ray tomography was performed by using an in-house-built X-ray microtomographic scanner JTomo in the X-ray tomography laboratory of the Department of Physics.

2.2. Synthesis of additive 1

[(Dodecylimino)bis(methylene)]bisphosphonic acid **1** was synthesized in three batches by dissolving phosphorous acid (44.5 g, 0.54 mol) and dodecylamine (50 g, 0.27 mol) into 400 ml of 6 M HCl. After heating the solution to reflux (>120 °C), an excess of 36 % formaldehyde (90 ml, 1.17 mol) was added to the solution dropwise within an hour after which the solution was refluxed for two more hours. The resulting white precipitate was filtered out and washed with ethanol. Because **1** is only soluble in basic aqueous solutions, NMR was measured in the presence of NaOH. Yield: 75 g, 46 %. Melting point: 210 °C. ^{1}H NMR (D_2O 300 MHz): δ 3.09–3.04 (m, 4H), 2.93 (d, 2H), 1.69–1.56 (m, 2H), 1.43–1.23 (m, 18H), 0.89 (t, 3H). ^{31}P NMR (D_2O 300 MHz): δ 14.16. Elemental analysis Calcd. for $C_{14}H_{33}NO_6P_2$: C, 45.04; H, 8.91; N 3.75. Found: C, 44.92; H, 9.21; N, 3.76.

2.3. 3D printing

The 3D model of the filters was designed using FreeCAD v. 0.16 and further processed into 0.1 mm layers with Slic3r v. 1.2.9. The 3D-printed filters were manufactured from the mechanically mixed powder, consisting of 70 wt-% of a powderous nylon-12 (particle size ca. 50 μm) and 30 wt-% of a finely grounded additive **1** (<125 μm), using selective laser

sintering 3D printing, which is a robust method to manufacture porous 3D-printed filters [37,45,47–49]. The laser power, speed, and printing temperature were set to 40 % (of 14 W), 1600 mm/s, and 172 °C, respectively. These parameters were selected to prevent the melting of the active additive **1** (mp 210 °C) while enabling the partial melting of nylon-12 particles in the printing process. Prior to the recovering and imaging experiments, the 3D-printed filters were thoroughly washed with water to remove any unsintered powder.

2.4. X-ray tomography

A filter was scanned inside a syringe before and after the adsorption tests. The voxel size of the 3D image was set to 8.1 × 8.1 × 8.1 µm to estimate the properties of the structure of the filter and simultaneously obtain a representative volume of the sample. The current and the voltage of the X-ray tube were set to 0.2 mA and 40 kV, respectively, and no additional filtering was used in the X-ray source to minimize the average energy of the X-ray spectrum of the source. The image size was 1374 × 1314 × 444 voxels in both cases, i.e., before and after the adsorption tests. In the reconstruction of the tomographic image, pi2 software was used [50]. The noise of the reconstructed images was reduced by using bilateral filtering and the segmentation of the pores was performed utilizing the Otsu thresholding method [51]. The pore size distribution of the sample was analysed within a selected 11.1 × 10.6 × 3.6 mm^3 volume using the tmap -function of the pi2 software, which calculates the local thickness map of the image [52].

2.5. Adsorption and desorption

The metals and their concentrations in the simulated mining waste solution were adjusted with a small modification according to the reported concentrations of metals observed in the biggest mine in Finland [53] and in aqueous mining waste [10,54]. Because REEs were of particular interest in the study, and because the AMDs of coal and ore mines typically contain 0–5 mg/l (0–5 ppm) and 5–25 mg/l (5–25 ppm) of REEs, respectively [55,56], the REE content of the analyte was set to 10 mg/l (10 ppm). The investigated mining waste solution was prepared by diluting the 10 000 mg/l stock solutions of Al, K, Cs, and Zn and 1000 mg/l standard solution of Sc, Fe, Co, Cu, Y, Nd, Dy, and U with 0.5 M H_2SO_4 to obtain an analyte solution containing 100 mg/l of Al, K, Ca, and Zn as well as 10 mg/l of Sc, Fe, Co, Cu, Y, Nd, Dy, and U. pH for the adsorption tests was set to 1–4 with 25 % ammonia solution. In the initial tests 5 ml of the solution, and in the longer adsorption tests 40 ml of the solution was withdrawn into a 60 ml syringe that was attached to a syringe pump. The flow rate of the pump was set to 90 ml/h and the simulated mining waste solution was passed through three stacked filters. Samples were taken every 5 ml to monitor the adsorption process, and pH was measured from each sample to confirm the stability of adsorption conditions. The amount of adsorbed metals was determined with Perkin Elmer ICP-OES Optima 8300 by measuring the metal concentration in the solution before and after passing the solutions through the 3D-printed filters. From these values, adsorption percentages were calculated with Eq. (1)

$$\text{Adsorption-\%} = \frac{c_i - c_f}{c_i} \times 100\% \quad (1)$$

where c_i is the metal concentration (mg/l) in the solution before adsorption tests, and c_f is the concentration (mg/l) in the solution after tests.

Desorption of the metals from the used filters was studied with 1, 3, and 6 M HCl, H_2SO_4, and HNO_3 by passing 30 ml of the acids through the filters with a flow rate of 15 ml/h. Desorption percentages were calculated with Eq. (2)

$$\text{Desorption-\%} = \frac{C_d \times V}{m_a} \times 100\% \quad (2)$$

in which C_d is the concentration of desorbed metals in the solution (mg/l), V is the volume of the acid passed through the filters (l), and m_a is the adsorbed amount of metals in the filters (mg).

2.6. Adsorption isotherms

The adsorption mechanism and capacity of the filters for Sc, Fe, U, Nd, Dy, and Y were determined by fitting their adsorption isotherms to linear Langmuir and Freundlich models [57,58]. Adsorption isotherms were determined in 0.5 M H_2SO_4 at pH 2 for Sc, Y, Nd, Dy, and U, and at pH 3 for Fe. For each metal 10, 50, 100, 250, 500, and 1000 mg/l solutions were passed through one filter at a time and the concentrations of both the initial eluent and final eluate were measured with ICP-OES. The total contact time for the adsorption isotherm tests was 1.5 h. All the tests were performed in triplicate. The results were plotted to the linear Langmuir adsorption isotherm Eq. (3) [57].

$$\frac{C_e}{Q_e} = \frac{1}{Q_{max}} C_e + \frac{1}{bQ_{max}} \quad (3)$$

where C_e is the concentration of the metals in the solution at equilibrium (mg/l), Q_e is the equilibrium loading of the metals (mg/g), b is Langmuir constant (l/mg), and Q_{max} is the maximum adsorption capacity (mg/g). The results were also fitted to the linear Freundlich adsorption isotherm Eq. (4) [58]

$$\log Q_e = \log K_f + \frac{1}{n} \log C_e \quad (4)$$

where K_f is the Freundlich isotherm constant (L/g) and n is constant indicating adsorption intensity. The capacity was calculated with respected to the amount of active material **1** in the filter.

2.7. Adsorption-desorption cycles

The reusability of the 3D printed filters was studied at pH 2 by performing five sequentially adsorption–desorption cycles for the three stacked filters. In the adsorption step, 40 ml of the mining waste solution was injected through the filters with a flowrate of 90 ml/h. The following desorption step was performed by injecting 30 ml of 6 M HNO_3 into the filters with a flowrate of 15 ml/h. Between the adsorption and desorption steps, the filters were washed with 10 ml of ultrapure water to remove metal and acid residuals on the surface of a syringe and tubing that could cause errors to the results and change the value of pH, respectively. The adsorbed and desorbed amount of metals in each cycle were determined as described above.

3. Results and discussion

3.1. Preparation, characterization, and structure of the 3D-printed filters

[(Dodecylimino)bis(methylene)]bisphosphonic acid **1** was synthesized by following the previously reported method by Moedritzer and Irani, where dodecylamine is reacted with phosphorous acid and formaldehyde in a one-pot acid-catalyzed reaction (Scheme 1) [29,59]. The resulting white solid, which started precipitating out from the

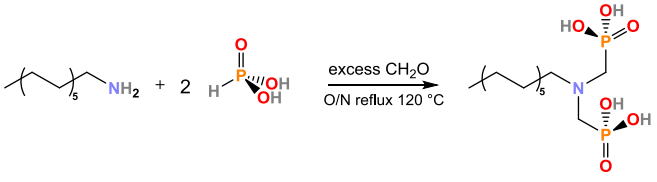

Scheme 1. Synthesis route for the [(dodecylimino)bis(methylene)] bisphosphonic acid **1** that was used as the active additive in the investigated 3D-printed filters.

solution when the heating was turned off, was filtered and washed with ethanol to remove HCl residuals. The purity of the compound was confirmed with ^{1}H and ^{31}P NMR (Figs. S1 and S2), elemental analysis (see above), and FTIR (see below). The active additive **1** was insoluble in both neutral and acidic aqueous solutions, in which the adsorption and desorption processes take place, but **1** dissolved into basic aqueous solutions (pH > 8).

The printing material for SLS printing was prepared by mixing 30 wt-% of the active additive **1** with the commercial nylon-12 powder. Nylon-12 was selected for the polymer matrix because it adsorbed only negligible amounts of the studied metals from the mining waste solution without the active additive (Table S1). A similar finding has previously been reported for nylon-12 although it adsorbed strongly and selectively Au [45]. The round 5 mm thick filters with a diameter of 16.6 mm (Fig. S3) were prepared using ShareBot SnowWhite SLS 3D printer. Each filter was cleaned thoroughly with deionized water to remove any unsintered powder before the experiments. Although the filters were 3D-printed the same way each time, variation in the distribution of the active additive inside filters may exist.

The micrometer-level structure and the distribution of the active additive inside the prewashed 3D-printed filter were analyzed by Helium Ion Microscopy (HIM) and X-ray tomography. The HIM images show that the porosity is homogeneous throughout the 3D-printed filter which is particularly visible from the HIM picture taken from the pure nylon-12 (Fig. 1). The porosity ensures that 3D-printed filters manufactured by the selective laser sintering contain voids and flow channels along which solutions can flow-through as previously reported [45,47,60]. Fig. 1 also shows that the aminomethylphosphonate additive **1** formed an adsorption layer on the surface of nylon-12 particles causing them to look more like plate-like particles than round-shaped ones as observed for the pure nylon-12. Importantly, prewash with the deionized water before imaging did not leach the active additive out from the filters. The negligible solubility of **1** in mineral acids and water at room temperature can contribute to its minimal dissolution during the adsorption and desorption steps, but it is more likely that the partially melting nylon-12 particles attached **1** to their surfaces during the 3D-printing process as depicted in Fig. 1. These are important findings because it is crucial that the active additive of the 3D-printed filters will remain intact during the recovery process and forms the adsorption layer which metal can coordinate to.

With X-ray tomography, the average porosity of the whole filter was determined to be 59 ± 2 % before the adsorption process and 60 ± 2 % after the adsorption indicating that there was no significant loss of material during the metal recovery process although leaching of some solids could sometimes be detected during the first millilitres of the adsorption tests. The average pore size was determined to be 95 ± 5 μm with a standard deviation of 50 μm and no significant difference was found in the pore size before and after using the filter. Similar pore sizes have previously been reported for 3D-printed filters utilized for recovering precious metals from electronic waste [37]. Fig. 2 shows that there were no significant changes in the structures of the unused and used filters. The ring-like structure was only marginally smaller in the used one, but otherwise no significant changes were detected. It should also be noted that the filter possibly moved a little during the adsorption process, and thus the image was not taken from the exactly same spot. Overall, HIM and X-ray tomography studies indicated that the filter has good porosity for the adsorption and desorption tests and the additive **1** is not leached from the filters in acidic aqueous solutions.

The 3D-printed filter was further characterized by a powder X-ray diffractometer (PXRD) and a FTIR-spectrometer, and its measured diffractogram and spectrum were compared to ones of the pure nylon-12 and the active additive **1**. The PXRD diffractogram of the pure nylon-12 filter was similar to the previously reported one [61], whereas the diffractogram of the 3D-printed filter containing both nylon-12 and **1** showed characteristic peaks of nylon-12 and **1** although some characteristic peaks of **1** were masked by the peaks of nylon-12 (Fig. S4). In the IR spectra of nylon-12 and the filter, the N—H stretch of the amide group was observed at 3291 cm^{-1} (Fig. 3). The less intense band at 3090 cm^{-1} in the IR spectrum of nylon-12 is the overtone of the C—N—H bend which was observed at 1540 cm^{-1}. This band was only barely visible in the spectrum of the filter, and no band was observed for **1**. The latter should not show the C—N—H bend because it is a tertiary amine [62,63], but depending on the pH, **1** can exist as a zwitterion [29]. The characteristic C═O stretch of nylon-12 at 1635 cm^{-1} was slightly shifted to 1633 cm^{-1} in the IR spectrum of the filter. Also, the asymmetric (2916 cm^{-1}) and symmetric (2848 cm^{-1}) stretching bands of CH_2 groups of nylon-12 shifted to 2919 cm^{-1} and 2850 cm^{-1} for the additive **1** and filter, respectively. The slight shifts of the CH_2 bands are expected because the additive and, therefore, the filter contain CH_3 groups which typically are observed at slightly higher wavenumbers than CH_2 groups [62,63]. The rocking of CH_2 group occurred at 719 cm^{-1} for nylon-12 and at 713 cm^{-1} for the additive **1** and filter [62,63]. Vibrations associated with P—OH stretch were observed at 2309 cm^{-1} for the additive **1** and at 2324 cm^{-1} for the filter. The additive **1** showed strong bands at 1154 cm^{-1} and 936 cm^{-1} which could be attributed to the asymmetric and symmetric stretch of the PO_3 group, respectively [64]. For the filter, these bands were shifted to 1157 cm^{-1} and 938 cm^{-1}. The bending of C—PO_3 groups was observed as a strong band at 585 cm^{-1} for the additive **1** and filter [65]. Overall, these findings supported the results obtained from the HIM and X-ray tomography studies and indicated that

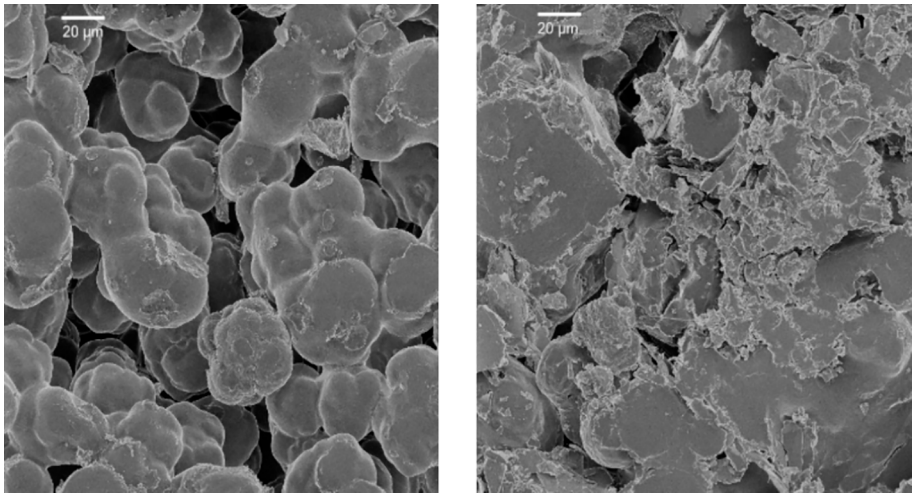

Fig. 1. HIM picture of the pure nylon-12 filter (left) and the filter with the additive **1** (right).

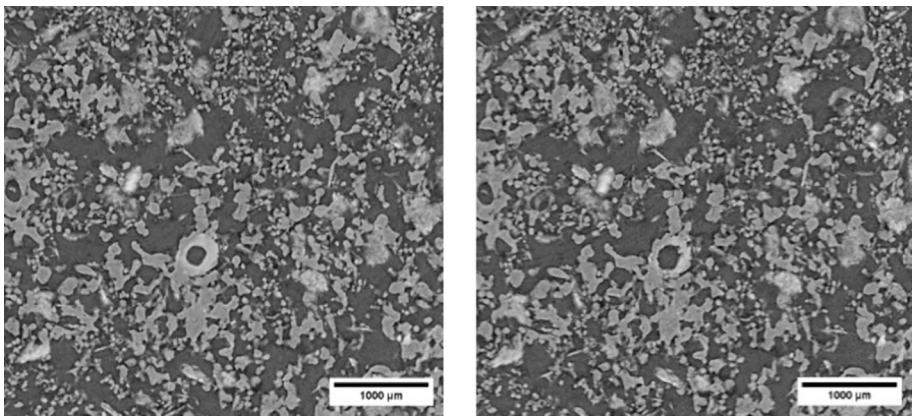

Fig. 2. X-ray tomography of the filter with the active additive **1** before metal adsorption test (left) and the same filter after the test (right).

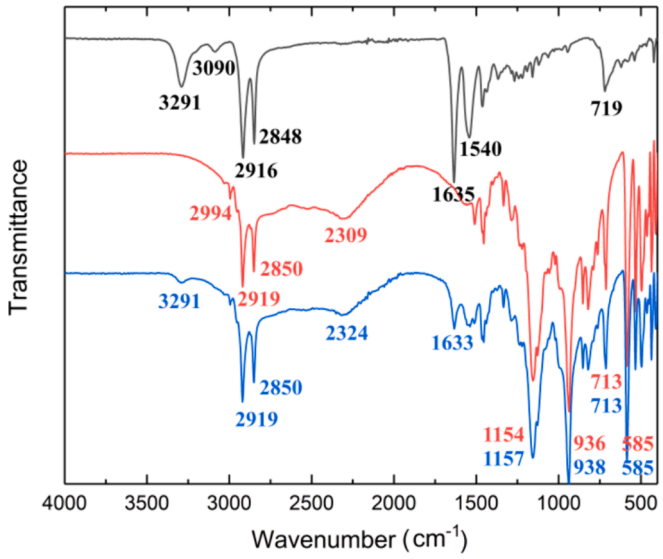

Fig. 3. FTIR spectra of nylon-12 (black), aminobisphosphonate additive **1** (red), and the 3D-printed filter (blue). (For interpretation of the references to colour in this figure legend, the reader is referred to the web version of this article.)

the active additive **1** inside in the 3D-printed filters did not decompose in the manufacturing process. In contrast to mineral acids and water, 2 M NaOH can leach a small amount of **1** out from the filters. Thus, the stability of **1** was further confirmed by recording the ^{1}H (Fig. S5) and ^{31}P (Fig. S6) NMR spectra of the leached active additive **1**. No signs of decomposition were observed in the recorded NMR spectra.

3.2. Metal adsorption

The adsorption tests were performed for the simulated mining waste solution containing 100 mg/l of Al, K, Ca, and Zn and 10 mg/l of Sc, Fe, Co, Cu, Y, Nd, Dy, and U in 0.5 M H_2SO_4. The solid-phase extraction system utilized in the study contained three stacked 3D-printed filters inside a 10 ml syringe and a syringe pump that was equipped with a 60 ml syringe (Fig. S7). The initial adsorption tests of the filters were performed by withdrawing 5 ml of the synthetic solution into the syringe and then injecting it through the three stacked filters with a flow rate of 90 ml/h. A pH range of 1 to 4 with an increment of 1 was studied to find out the effect of pH on adsorption. In this pH range, the protonation degree of the hydroxy groups (—OP(**OH**^{x})$_2$, x = 1 or 2) of phosphoric acid **1** varies from 0 % to 100 % which was determined by using the Henderson-Hasselbalch equation [66] and the previously reported pKa values of 1.33 and 5.55 for the first and second protonation, respectively, of the similar aminobisphosphonic acid (Table 1) [29]. The leaching of **1** was monitored by measuring the phosphorus concentration of the samples during the adsorption studies. It was found to be minimal (<1 %) indicating no loss of the active additive **1** in the process.

The adsorption of each metal increased with increasing pH value (Fig. 4). Of all adsorbed metals, Sc adsorbed most strongly. Roughly 80 % of Sc was already adsorbed at pH 1, whereas the adsorption percentages for Fe and U were ~ 35 %, and for Y, Nd, and Dy they were less than 10 % at the same pH value (Fig. 4). No adsorption of Al, K, Ca, Co, Cu, or Zn was detected at pH 1. A similar but stronger trend was observed at pH 2, where 96 % of Sc, ~75 % of U and Fe, and >20 % of Y, Nd, and Dy were adsorbed by the filters, but no significant adsorption of other metals was observed. However, when the pH value was increased from 3 to 4, the adsorption percentages increased from 22 % to 50 % for Al, from 14 % to 46 % for Cu, from 9 % to 35 % for Zn, and from 1 % to 5 % for Co. No significant adsorption of K and Ca was detected at pH 3 or pH 4. The adsorptions of Sc, Fe, Y, Nd, Dy, and U were strong at pH 3 and practically quantitative at pH 4. The efficient and selective adsorption of Sc and U by bisphosphonic acid-based adsorption materials in the presence of other metals has been reported before [32,67], but the above results demonstrated that the 3D-printed filters can also effectively adsorb other REEs (Y, Nd, and Dy) like commercial aminophosphonic acid resin, Purolite S950, that adsorbs La, Sm, and Ho well [35]. However, the coadsorption of Al with REEs (Sc, Y, Nd, and Dy) in percentages was much smaller for the investigated 3D-printed filters than for Purolite S950, which adsorbed Al equally or stronger if compared to the adsorption of Ho and La, respectively. It should be mentioned that the result obtained for Fe at pH 4 should be interpreted with caution because roughly 30 % of Fe precipitated out from the solution as a brown solid (most likely as FeOOH) [68] when the value of pH was increased to 4. This solid was filtered from the solution before the adsorption tests were continued. Moreover, while the adsorption percentages for Al and Zn were not high in the studied pH range, their adsorbed amounts in micrograms were high due to their high initial concentrations in the mining waste solution. For example, the adsorption for Al at pH 3 was 56.7 ± 12.5 µg, whereas for Sc and Dy they were 32.3 ± 9.1 µg and 26.8 ± 5.8 µg, respectively.

To investigate the saturation limit of the three stacked 3D-printed filters, 40 ml of the synthetic solution was passed through them, and samples were taken every 5 ml. As already explained above the filters

Table 1
Degree of protonation for the P-OH groups of **1** at pH values of 1–4.

pH	1	2	3	4
OH^{1}	68 %	18 %	2 %	0 %
OH^{2}	100 %	100 %	100 %	97 %

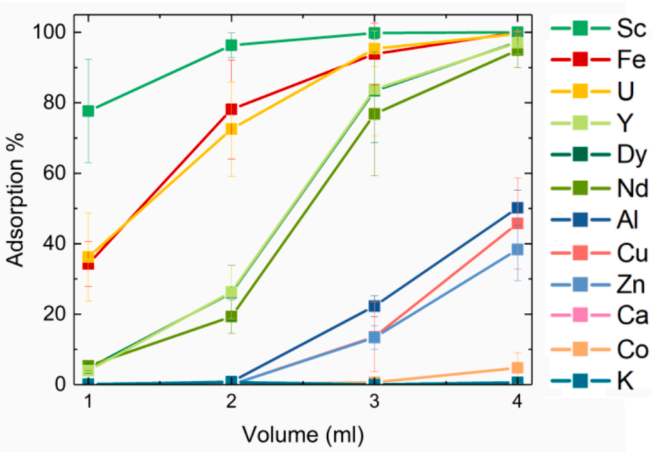

Fig. 4. Avarage adsorption percentages and their standard errors for the eluted metals in a function of pH (1–4) when 5 ml of synthetic solution is passed through the filters.

adsorbed Sc, Fe, and U better than the rest of the investigated metals. However, the adsorption of these three metals quickly decreased after the first 5 ml of the mining waste solution was passed through the three filters in the pH regime of 1–3 and passing more than 40 ml of the solution through the filters decreased the adsorption percentages below 20 % for each metal (Fig. 5). In contrast to this, at pH 4, the saturation was not achieved even after 40 ml of the solution was passed through the three filters and the adsorption percentages remained over 60 % for Sc and Fe, over 40 % for U, and over 20 % for Y, Nd, and Dy. The adsorption percentages of the less adsorbed metals, namely Al, Cu, and Zn followed by K, Ca, and Co, also increased in pH 4 if compared to the lower pH values, but their adsorption percentages were ~10 % or less when more than 20 ml of the mining waste solution was passed through the filters.

Overall, the results of adsorption studies indicated that in a low pH value of ~1, Sc, U, and Fe could be selectively recovered from the investigated mining wastewater, although their total adsorption percentages remained rather low and passing more than 40 ml of the solution through the three filters in the pH regime of 1–3 was not reasonable. However, if the aim is to recover Y, Nd, and Dy from the mining waste solution, higher than pH 1 should be used in the adsorption process.

3.3. *Adsorption isotherms and adsorption capacities for Sc, Fe, Y, Nd, Dy, and U*

The adsorption isotherms were fitted to linear Langmuir (Eq. (3)) and Freundlich (Eq. (4)) models to get more insight into the capacities of the filters and the adsorption mechanism of the studied metals. The Langmuir adsorption isotherm describes the equilibrium between an adsorbate and a monolayer adsorbent surface with equal binding sites and energies [57], whereas the Freundlich adsorption isotherm describes multilayer adsorption to a heterogenous surface which binding sites and energies can differ from one to other [58,69]. The adsorption isotherms were determined for Sc, Fe, Y, Nd, Dy, and U from samples whose concentrations ranged from 10 to 1000 mg/l either at pH 4 (Sc, Y, Nd, Dy, and U) or at pH 3 (Fe), due to the excessive precipitation of Fe at pH 4. This means that the results obtained for Fe are not directly comparable to the results of other metals. The maximum adsorption capacities (Q_{max}) determined from the Langmuir adsorption isotherms were calculated with respect to the amount of the active additive **1** in the filter. All tests were performed with three replicates and the results were displayed as a mean with a standard deviation of the replicates. For all other metals, except for Fe, the adsorption isotherms were fitted to the Langmuir model with decent correlations of $R^2 = 0.97–0.99$, while the correlation of Fe was only $R^2 = 0.89$ (Table 2 and Fig. S8). However, the adsorption isotherms of Fe were well fitted to the Freundlich model with the correlation of $R^2 = 0.99$ (Table 2 and Fig. S9). The Freundlich model also showed an equally good correlation for Sc than for Fe, while for Y, Nd, Dy, and U statistically meaningful results were not obtained according to the F-tests. All determined parameters along with their errors from the adsorption isotherm fits are presented in Table 2.

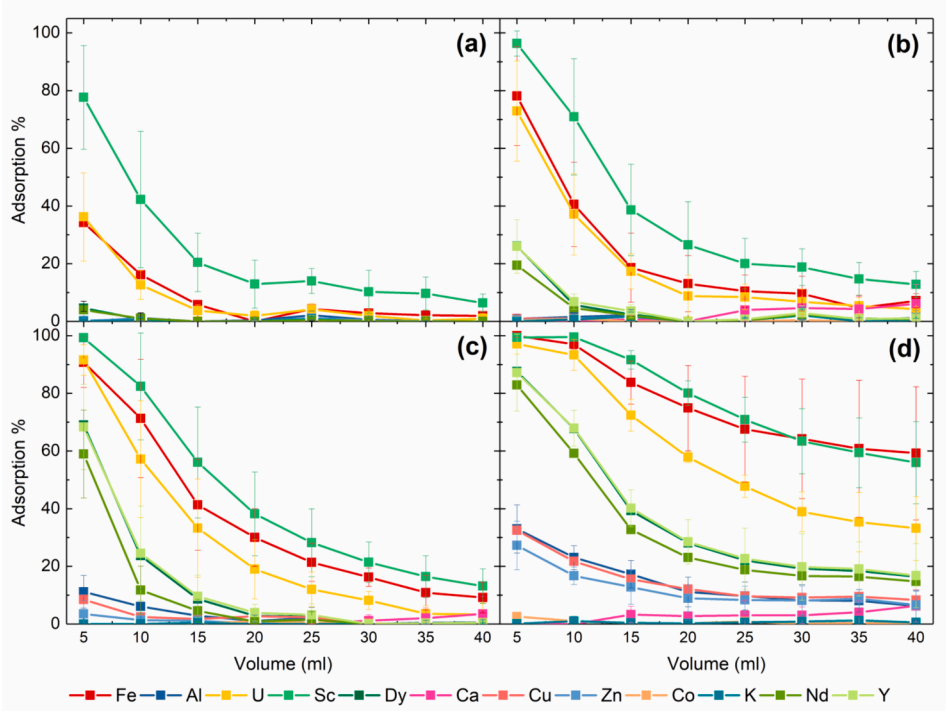

Fig. 5. Average adsorption percentages and their standard errors at pH values of 1–4 for every 5 ml of the synthetic solution passed through the filters at pH 1 (a) pH 2 (b), pH 3 (c), and pH 4 (d). The adsorption tests were performed in triplicate.

Table 2
Calculated maximum adsorption capacities Q_{max}, Langmuir constants b, Freundlich constants K_f and n, and correlation coefficients for the linear fittings for Sc, Fe, U, Dy, Nd, and Y.

Element	Langmuir					Freundlich	
	Q_{max}mg/g	Q_{max}mmol/g	bL/mg	R^2	K_f $mg^{1-n}L^n/mg$	n	R^2
Sc	22.86 ± 3.61	0.51 ± 0.08	0,018 ± 0,002	0.970 ± 0.006	4.10 ± 1.01	4.15 ± 0.71	0.994 ± 0.005
Fe*	–	–	–	0.887 ± 0.041	1.57 ± 0.41	1.98 ± 0.18	0.997 ± 0.003
U	111.65 ± 3.77	0.47 ± 0.02	0.036 ± 0.004	0.985 ± 0.001	–	–	0.776 ± 0.028
Dy	37.84 ± 6.45	0.23 ± 0.04	0.030 ± 0.018	0.975 ± 0.018	–	–	0.743 ± 0.033
Nd	34.60 ± 2.11	0.24 ± 0.01	0.024 ± 0.005	0.979 ± 0.003	–	–	0.798 ± 0.023
Y	14.74 ± 2.84	0.17 ± 0.03	0.030 ± 0.008	0.996 ± 0.004	–	–	0.794 ± 0.019

* Determined at pH 3.

The highest adsorption capacity was determined for U (111.65 mg/g), followed by Dy (37.84 mg/g), Nd (34.60 mg/g), Sc (22.86 mg/g), and Y (14.74 mg/g). No adsorption capacity was determined for Fe because the Langmuir model did not fit well the adsorption isotherms of Fe. Because elements with higher molar masses have naturally higher capacities in mg per g than lighter ones, the adsorption capacities were also converted to mmol per g. When the values in mmol per g were examined, it was found that Sc had the highest adsorption capacity of 0.51 mmol/g among all investigated metals, whereas the values for U, Nd, Dy, and Y were 0.47, 0.24, 0.23, and 0.17 mmol/g, respectively. The data indicates that the 3D-printed filters can adsorb U almost as effectively as Sc in mmol per g. Although the determined maximum adsorption capacities for the investigated 3D-printed filters are decent, they are smaller than the highest ones reported for other similar adsorbents and ion-exchange resins. For example, almost three times larger maximum adsorption capacity of U (1.31 mmol/g) has been reported for synthesized aminophosphonate resins [70]. The capacity for Sc is higher than what has been reported for mesoporous silica (1 mg/g) [71], but lower than the capacity of commercial aminophosphonate functionalized resin that is 35.5 mg/g (dry resin) at pH 1.5 [72]. The adsorption capacity of Nd was 70.1 mg/g for aminophosphonate functionalized metal–organic framework [73], and the adsorption capacities of 104.1, 118.0 and 63.9 mg/g were reported for Nd, Dy, and Y, respectively, when phosphorylated phenolic resins where used as adsorbents [74]. Theoretical adsorption maximums for the 3D-printed filters containing 30-wt% of the active additive **1** were calculated by assuming that metals bind to **1** with 1:1 ratio. The calculated values were 120.4 mg/g for Sc, 238.0 mg/g for Y, 386,0 mg/g for Nd, 435,3 mg/g for Dy and 637.4 mg/g for U which were considerable higher amounts than what were obtained from the experimental data. The differences between the 3D-printed filters and previously reported adsorbents and ion-exchange resins most likely originate from the fact that there is only 30-wt% of the active additive **1** in the 3D-printed filters and/or likely only some of the active additives on the surfaces of nylon-12 particles are available for binding as suggested by the theoretical maximum capacities.

3.4. Adsorption mechanism and selectivity of 3D-printed filters

Given that the 3D-printed filters contain aminophosphonic acid **1** as an active additive, they should function like a chelating ion exchange resin in which adsorption kinetics are dictated by the formation of a coordination bond between the functional groups of an active additive and metal ions [35,75–77]. To get more insight into the adsorption mechanism and selectivity of the 3D-printed filters, we utilized the above-described Langmuir (Eq. (3)) and Freundlich (Eq. (4)) models as well as FTIR spectroscopy.

The good fits of adsorption isotherms of Y, Nd, Dy, and U to the Langmuir model indicated that they likely bind only to one adsorbent site of the active additive **1**. The result is in par with the assumption that the active additive **1** forms (mono)layer on the surfaces of nylon-12 particles to which metals can coordinate. The data also showed that the 3D-printed filters adsorbed U stronger than Y, Dy, and Nd because the determined Langmuir constants b for U, Y, Dy, and Nd were in descending order: 0.036, 0.030, 0.030, and 0.024 L/mg, respectively. Because the larger Langmuir constant b is associated with the stronger interaction between the adsorbate and the adsorbent [78], the above data also explained the stronger selectivity of the 3D-printed filters towards U over Y, Nd, and Dy. Contrast to Y, Nd, Dy, and U, the adsorption isotherms of Sc and Fe fitted better to the Freundlich than to the Langmuir model implying that the adsorption mechanism of Sc, and in particular of Fe, might differ from Y, Nd, Dy, and U. It should be noted that the fit of the adsorption isotherm of Sc to the Langmuir model was reasonably good, so the nature of the adsorption mechanism of Sc cannot be unambiguously determined from two different fits. Because the metal–ligand coordination is controlled by several factors, such as the geometry and energy of the bonding orbitals [77], it is difficult to say a specific reason for the different adsorption mechanisms. Because the Freundlich model indicates the multilayer adsorption mechanism, the active additive **1** could bind more than one Sc or Fe ion per adsorbent site, due to their smaller ionic radii compared to Y, Nd, Dy, and U [79], and/or the coordination mode of **1** with Sc and Fe could differ from Y, Nd, Dy, and U. Although aminophosphonic acids usually bind the trivalent metal ions via the phosphonate oxygen atoms, their coordination modes with different metals can differ [80,81]. Unfortunately, no direct evidence was obtained for either case from FTIR spectroscopy studies (see below). Importantly, the fitted Freundlich constant K_f, the distribution coefficient which indicates similarly to b the interaction between the adsorbate and the adsorbent [82], was larger for Sc than for Fe. The result was in line with the adsorption studies and proved that the 3D-printed filters adsorbed stronger and more selectively Sc than Fe.

Because the adsorption isotherms were only determined for the best adsorbing metals, the stronger selectivity of the 3D-printed filters towards Fe, REEs, and U over other investigated metals will only be discussed at a qualitative level. The adsorption percentages and capacities of the studied metals mainly followed the strength of their effective Lewis acidities whether they are determined from Gutmann–Beckett-type [83], fluorescent [84,85], or ESR [86] measurements. The Lewis acidity of the two strongest adsorbed metals, Sc and U, is strong which is further augmented by their strong oxophilicity [87]. Unfortunately, references 83–86 report no data for Fe, which was adsorbed as strongly as U by the 3D-printed filters. However, a previous study has shown that the simple aminobisphosphonates coordinate stronger to Fe than Nd in aqueous media [81], although Fe is not calculated to be as oxophilic as lanthanoids [65]. For the remaining well-adsorbed metals—Al, Cu, Zn, Y, Nd, and Dy—the reported effective Lewis acidities are similar in strength [83–86], but REEs are more oxophilic than Al, Cu, and Zn, which most likely facilitates their adsorption to the investigated filters over Al, Cu, and Zn [87], if the phosphonic acid groups of **1** play the largest role in the adsorption mechanism. To find out this, FTIR spectroscopic studies were carried out for the unused and used filters.

The FTIR spectra of the 3D-printed filters were measured after passing the mining waste solution and the solutions containing either Sc, Nd, or U through the filters at pH 4 until the capacity of the filters was reached (~100 ml). Unfortunately, only small shifts (less than 1 cm^{-1})

were observed in the vibration bands when the measured spectra of the used and unused filters were compared together (Figs. S10–S13). Although the shifts associated with the vibration bands of phosphonate groups upon coordination can be very small for aminophosphonate and aminophosphonic acids [80], the role of the phosphonate groups in the adsorption mechanism cannot be determined based on such small shifts. Zhao *et al.* have reported the FTIR spectra of aminophosphonate extractant where the shifts of vibration bands were only detected when the extractant was fully loaded with Yb^{3+} [88]. Given that the maximum adsorption capacity of the 3D-printed filters is reached before the full deprotonation of phosphonic acid groups and the amount of the active additive is only 30-wt% in the filters (see above), it is possible that more intense vibration bands of the nylon-12 matrix and/or unoccupied phosphonic acid groups mask the characteristic shifts arising from the coordination of metal ions to the phosphonic acid groups. A slightly more indicative proof of the metal coordination to the phosphonic acid groups of **1** was observed in the intensity of P-OH stretches observed at $\sim$ 2324 cm^{-1}; it slightly decreased upon metal coordination (Fig. S14). Indeed, a similar decrease in the intensity or complete removal of P-OH stretches has been reported for aminophosphonates and aminophosphonic acids upon coordination to a metal ion [80].

Although the direct shifts of the functional groups and changes in the intensities of vibration bands were rather uninformative, three facts supported the role of the phosphonate groups in the adsorption mechanism. First, the adsorption tests performed for the 3D-printed filters consisting only of pure nylon-12 showed very limited adsorption, almost negligible within the margin of errors, towards any of the investigated metals (Table S1). Second, the adsorption of all investigated metals increased in tandem with the increasing pH as the deprotonation degree of the phosphonic acid group increased (Table 1). The ion exchange mechanism is pH-dependent [89,90]. Third, XPS measurements performed for the aminophosphonate-based sorbents showed that phosphonate groups in conjunction with amine groups play an important role in the sorption process of REEs [91]. Taking into account all the above mentioned, it is highly likely that the adsorption process is dictated by the phosphonic acid groups of the active additive **1** in the investigated 3D-printed filters and that the functional groups of nylon-12 play only a minor role.

3.5. Mineral acid elutions

Three different mineral acids, namely HNO_3, H_2SO_4, and HCl, with three different molarities 1, 3, and 6 M were investigated as eluents in desorption studies. 30 ml of the eluent was used in each desorption experiment and the experiments were performed for the filters utilized in adsorption tests at pH 3 and 4, where the adsorptions of metals were stronger compared to pH 1 and 2. With 1 M acids generally less than 50 % of the adsorbed metals were eluted out from the filters and the desorption of Y, Nd, and Dy was only 30–40 % (Fig. S15). Minimal amounts ($\sim$6 %) of Fe and U were eluted out from the filters with 1 M acids. Increasing the molarity from 1 M to 3 M resulted in higher elution percentages. For example, 50–75 % of Y, Nd, and Dy were eluted with all 3 M acids, and the percentages for Fe and U increased to 11 % and 7 %, respectively, with 3 M HCl, whereas with 3 M H_2SO_4 increase were 18 % and 8 %, respectively. In contrast to 3 M HCl and H_2SO_4, the elution percentages of 3 M HNO_3 for Fe and U remained rather low (<5 %). With 6 M mineral acids over 90 % of Y, Nd, and Dy were desorbed from the filter, while the desorption of Fe and U remained low. For Fe and U, the best-performing 6 M acid was H_2SO_4 which was able to recover 20 % of Fe and 50 % of U from the filter indicating that these metals can also be eluted to some extent. All the used acids also eluted a significant amount of Zn and Ca from the filters in terms of milligrams and percentages. Therefore, the adsorption of these two metals should be minimized if the aim is obtain a high-purity REE fraction. The elution percentages of Al and Co also improved when the molarity of the acid was increased. However, the total amount of eluted Co in milligrams was low because it was poorly adsorbed by the filters (see above). The eluted amount of Cu increased with increasing molarity of HNO_3 but with HCl, it remained similar (73–78 %) despite the increase in molarity. H_2SO_4 was also able to remove Cu effectively from the filters. In contrast to all other metals, Sc remained in the filter regardless of the used eluent most likely because of its strong Lewis acidity and oxophilicity. Only 6 M HCl was able to desorb a small amount of Sc ($\sim$2 %), but with all other acids, the elution percentage for Sc was less than 1 %. Overall, Y, Nd, and Dy were desorbed from the filters well, but no clear selectivity towards metals or any group of metals was observed in the elution studies. In principle, only Fe and U could be eluted to their own fraction with H_2SO_4 if other metals are first washed out with HNO_3 or HCl.

3.6. The recovery process for REEs

The adsorption and desorption studies described above demonstrated that the 3D-printed filters selectively adsorbed Sc, Fe, Y, Nd, Dy, and U below pH 2, but no selectivity was observed in the desorption studies, except for Fe and U. The three tested mineral acids particularly eluted Al, Ca, and Zn, which were adsorbed by the filters over pH 2. Thus, to minimize the contamination of the final REE-rich eluate with other metals, the sequential recovery process for Y, Nd, and Dy was developed at pH 2. The flow chart of the developed recovery process is depicted in Fig. 6, and the amounts of adsorbed and desorbed metals in each step of the process are also given in Tables S2 and S3. In the recovery process, 40 ml of the synthetic mining waste solution in 0.5 M H_2SO_4 was passed through five sets of the three stacked 3D-printed filters and samples for ICP-OES measurements were taken from each fraction. The adsorbed metals were eluted with 6 M HNO_3 to minimize the amount of Fe and U in the final eluate that mainly consisted of Al, Y, Nd, and Dy.

During the first two steps of the process, Sc and Fe were completely removed from the mining waste solution. Already at the first step, 350 $\pm$ 10 μg (95 %) of Sc and 290 $\pm$ 50 μg (76 %) of Fe were adsorbed from the solution, and the second step recovered the rest of Fe and traces of Sc. For U, however, three steps were necessary for its complete removal from the solution. During the first two steps, 250 $\pm$ 30 μg (69 %) and 100 $\pm$ 40 μg (86 %) of U were adsorbed, and the rest of it ($\sim$20 μg, 100 %) was finally adsorbed in the third step. The first three steps also adsorbed 318 $\pm$ 6 μg of Y (84 %), 372 $\pm$ 6 μg of Nd (93 %), and 352 $\pm$ 1 μg Dy (92 %). However, for complete removal of Nd and Dy, four steps were required, whereas for Y all five steps were needed. Most of K, Ca, Co, Cu, and Zn passed through the filters during the five adsorption steps because less than 20 % of K, Ca, and Co, 25 % of Zn, and 30 % of Cu were adsorbed into the filters. Interestingly, K starts to adsorb only in the last (i.e. fifth) step of the process, after stronger adsorbed metals are removed from the mining waste solution. In contrast to K, Ca, Co, Cu, and Zn, the adsorption of Al was significant, and particularly increased after Sc was removed from the mining waste solution. In total, 1460 $\pm$ 197 μg (48 %) of Al was adsorbed in the process. The high adsorbed amount of Al could be problematic in the elution steps because it can contaminate the final REE-rich eluate. Fortunately, the strong adsorption of Al is compensated by its weaker desorption if compared to Y, Nd, and Dy in the desorption steps (see below).

When the first-step filters were eluted with 6 M HNO_3, 110 $\pm$ 26 μg of Nd (84 %), 94 $\pm$ 20 μg of Dy (77 %) and 80 $\pm$ 16 μg (77 %) of Y were desorbed from the filters along with 90 $\pm$ 15 μg (52 %) of Al. Eluting the second-step filters yielded to similar results because 90 % of adsorbed Y, Nd, and Dy as well as 54 % of adsorbed Al were eluted from the filters. The coadsorption and desorption of Al alongside REEs has been reported to be an issue in the separation processes when aminophosphonic acids have been utilized [33–35]. However, it is worth mentioning that the two sequenced adsorption and desorption steps result in the elute in which equal amounts of Nd, Dy, Y, and Al are present. This is a significant result because the concentration of Al in the unprocessed simulated mining waste solution is ten times higher than the concentrations

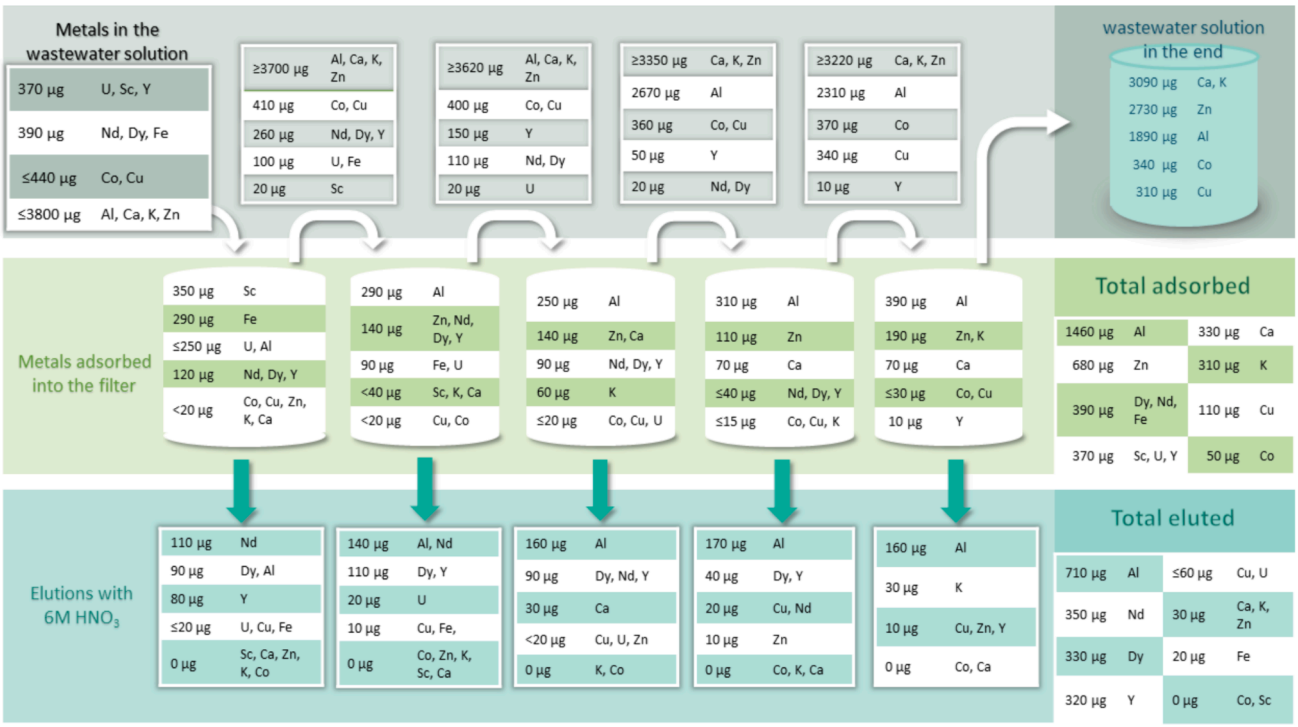

Fig. 6. Sequential five-step adsorption and desorption process developed for recovering Sc, Fe, and U as well as concentrating Y, Nd, and Dy into their own less complex fractions at pH 2. The top, middle, and bottom figures show the concentrations of metals in the solution, in the 3D-filters, and in eluate, respectively, after each step of the process along with the total amounts.

of Y, Nd, and Dy. Only a small amount (<20 µg) of each Cu, Fe, and U was washed out from the filters with 6 M HNO_3 in the first and second elution steps, as expected.

Over 95 % of the adsorbed Y, Nd, and Dy was desorbed during the elution of the third-step filters, but unfortunately, the amount of desorbed Al also increased and exceeded the amount of Y, Nd, and Dy. Eluting the fourth and fifth sets of filters yielded elutes that mostly contained 170 ± 20 µg and 160 ± 10 µg of Al, respectively. Only minor amounts of other metals than Al, Y, Nd, and Dy were desorbed during the third, fourth, and fifth elution steps. Fig. 7 summarizes the amount of adsorbed and desorbed metals in the sequential five-step recovery process. It is evident from Fig. 7 that complete adsorption of Sc, Fe, U, Nd, Dy, and Y was achieved and that Y, Nd, and Dy were desorbed from the filters alongside Al with 6 M HNO_3. This yielded the final eluate which consisted of 91 % of three REEs (Y, Nd, and Dy; 53 %) and Al (38 %) as well as 9 % of other metals (Fig. S17).

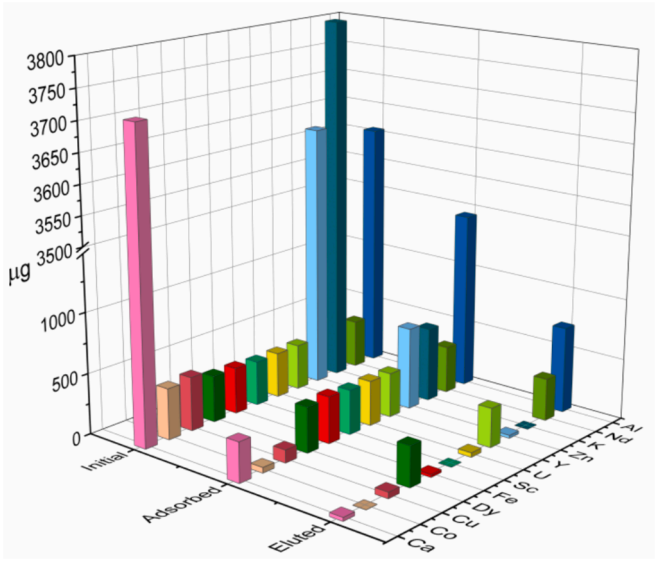

Fig. 7. The total amount of metals adsorbed and eluted during the sequential five-step recovery process. Close-up view of initial, adsorbed, and eluted amounts of metals with the lower initial concentrations are given in Fig. S16 and total percentages in Fig. S17.

Based on the results above, to obtain the pure REE fraction from the mining waste solution, three sequential sets of three stacked 3D-printed filters would be enough because these adsorb as much as 84–100 % of REEs from the mining waste solution. Only two sequential adsorption steps could also be considered if Al desorption must be minimized in the subsequent elution steps. Even though Fe and U were adsorbed strongly in the first steps of the process, they did not extensively contaminate the final REE-rich fraction because only a minimal amount of these two metals was desorbed from the filters with 6 M HNO_3. However, Fe and U can, to some extent, be desorbed from the filters with 6 M H_2SO_4 after elution with 6 M HNO_3, unlike Sc which was not desorbed in significant amounts from the filters with any of the investigated acids. When the total amounts of the most desorbed metals—Al, Y, Nd, and Dy—in the final eluates are compared to their initial concentrations, the results showed that 17 % of Al, 82 % of Y, 85 % of Nd, and 89 % of Dy were recovered with the investigated sequential five-step recovery process. Moreover, no coadsorption of Ca, which has been an issue in the previously reported study, was observed [31].

Because of the accumulation of Sc, Fe, and U into the filters, it was necessary to study the reusability of the filters. Thus, five sequential adsorption–desorption cycles were performed for the three stacked filters by injecting 40 ml of the mining waste solution with pH 2 through them with a flowrate of 90 ml/h followed by the elution step with 30 ml of 6 M HNO_3 similar to the five-step recovery process. It was evident from the results that the adsorption of Y, Nd, and Dy already decreased after the first cycle and was non-existent in the fifth cycle due to the accumulation of Sc, Fe, and U into the filters (Fig. S18). Thus, the presence of Sc, Fe, and U in the mining waste solution compromised the

reusability of the filters. However, these three metals can be removed from a multimetal solution by a simple precipitation step leaving most of Y, Nd or Dy in the solution as demonstrated in the previous studies [29,92]. When the reusability test was performed for the mining waste solution containing no Sc, Fe, and U, a small increase in the adsorption of Y, Nd, and Dy was observed in the first cycle, but it levelled out at the same level as in the five-step recovery process over the next four cycles (Fig. S19). The better adsorption rate of Y, Nd, and Dy in the first cycle most likely originated from the absence of Sc, Fe, and U in the solution. Although the accumulation of Al was also detected in the data (Fig. S19), it did not affect the adsorption and desorption of Y, Nd, and Dy during the five sequential cycles. The result confirmed that the filters are reusable if the most accumulating metals are removed from the multimetal mining waste solution.

Comparing the recovery rate of the developed five-step recovery process to other adsorption methods developed for the recovery of the REEs from acidic mine waste waters, it can be concluded that the obtained recovery rates of the 3D-printed filters are similar to the selected adsorbents functionalized with aminophosphonic acid and/or sulfonic acid and/or amide groups (Table 3).

Overall, the results obtained in this study not only highlighted the efficient recovery of the REEs from the mining waste solution but also confirmed that the amount of Al can be significantly decreased in the final REE-rich eluate of the mining waste solution, while the coadsorption and desorption of Ca can be eliminated. These novel results are important because the coadsorption and desorption of Al and Ca alongside with REEs have been reported to be an issue in previous studies [33–35].

4. Conclusions

Recovery of Y, Nd, and Dy from the simulated mining waste solution containing multiple metals was studied with the aminophosphonic acid **1** functionalized 3D-printed filters. The structure of the filters was studied in detail with HIM and X-ray tomography imaging which revealed that the filters have uniform structure, even distribution of the additive **1**, and a good porosity for the recovery process. The FTIR, powder X-ray, and NMR studies performed for the pure nylon-12, the active additive **1,** and the 3D-printed filters showed that the active additive stays intact in the printing process as well as during the recovery process. The adsorption of the investigated metals from the simulated mining waste solution was studied at pH 1–4 in which additive **1** exists in two different protonation states. The highest recovery rates were obtained at pH 4. However, the separation between REEs and the other elements present in the mining waste solution was best at pH 2. Desorbing the metals from the filters was studied with 1, 3, and 6 M HNO_3, HCl, and H_2SO_4. In general, the 6 M acids were the best eluents as they desorbed $\geq$ 90 % of the adsorbed Y, Nd, and Dy. The sequential five-step recovery process for Y, Nd, and Dy worked the best at pH 2 and yielded the final eluate that mainly contained Al, Y, Nd, and Dy. Importantly, the recovery process significantly decreased the amount of Al in the final eluate compared to its initial concentration in the mining waste solution and fully eliminated the coadsorption and desorption of Ca with Y, Nd, and Dy. The reusability tests showed that the accumulation of the best adsorbing metals, Sc, Fe, and U, into the filters compromised their reusability in the recovery of Y, Nd, and Dy, but by removing these three accumulating metals from the solution before the recovery process, the reusability of the filters can be maintained. The capacity of the filters towards Sc, Y, Nd, Dy, and U was determined by fitting their adsorption isotherms to the Langmuir model. The best capacity was determined for Sc (Q_{max} = 0.51 mmol/g) followed by U, Nd, Dy, and Y with capacities of 0.47, 0.24, 0.23, and 0.17 mmol/g, respectively. Interestingly, the fitting of the adsorption isotherms to the Langmuir and Freundlich models indicated that the adsorption mechanism of Fe (and also Sc) might be different from the one of Y, Nd, Dy, and U. Considering all the abovementioned, the 3D-printed filters with aminophosphonic acid **1** as an active additive showed promise for the recovery and separation of Y, Nd, and Dy from the multimetal mining waste solution. The next logical step is to improve the capacity and selectivity of the developed 3D-printed filters towards REEs as well as to develop better elution methods for Sc, Fe, and U.

Table 3
Selected adsorbents used for the recovery of the REEs from acidic mining waste solutions.

Adsorbent	REE adsorption %	REE desorption %	Ref
Aminobisphosphonate	100 %	>82 % (−Sc)	This work
TP260(aminophosphonic)	80–100 %	>95 %	[33]
S950(aminophosphonic)	100 %	<80 %	[34]
Aminophosphonate functionalized silica	<80 % (Eu)	90 %	[93]
Lewatit MDS200H(Sulfonic acid)	85 %	89 %	[94]
Lewatit MDS200H(Sulfonic acid)	78 %	75–100 %	[95]
Amide functionalized silica	>75 %	>75 %	[96]

Author contributions

All authors have given approval to the final version of the manuscript.

CRediT authorship contribution statement

Emilia J. Virtanen: Writing – review & editing, Writing – original draft, Visualization, Validation, Investigation, Formal analysis, Conceptualization. **Esa Kukkonen:** Writing – review & editing, Resources, Investigation. **Janne Yliharju:** Resources. **Minnea Tuomisto:** Formal analysis, Investigation. **Janne Frimodig:** Resources. **Kimmo Kinnunen:** Visualization, Resources, Investigation. **Elmeri Lahtinen:** Writing – review & editing, Conceptualization. **Mikko M. Hänninen:** Writing – review & editing, Conceptualization. **Ari Väisänen:** Writing – review & editing, Supervision, Funding acquisition, Conceptualization. **Matti Haukka:** Writing – review & editing, Supervision, Resources, Conceptualization. **Jani O. Moilanen:** Writing – review & editing, Writing – original draft, Visualization, Supervision, Resources, Project administration, Funding acquisition, Data curation, Conceptualization.

Declaration of competing interest

The authors declare that they have no known competing financial interests or personal relationships that could have appeared to influence the work reported in this paper.

Data availability

Data will be made available on request.

Acknowledgment

We thank the University of Jyväskylä, the Research Council of Finland (projects 315829 and 338733), the Technology Industries of Finland Centennial Foundation and Jane and Aatos Erkko Foundation for their financial support. We would like to acknowledge laboratory engineer Elina Hautakangas for carrying out elemental analyses for the samples and research assistant Tia Christiansen for performing part of the ICP-OES measurements and laboratory work, and Anssi Peuronen (University of Turku) for the useful discussions related to the subject.

Appendix A. Supplementary material

Supplementary data to this article can be found online at https://doi.

org/10.1016/j.seppur.2024.128599.

References

[1] Waste statistics, n.d., https://ec.europa.eu/eurostat/statistics-explained/index.php?title=Waste_statistics#Total_waste_generation (accessed October 26, 2023).

[2] É. Lèbre, G.D. Corder, A. Golev, Sustainable practices in the management of mining waste: a focus on the mineral resource, Miner. Eng. 107 (2017) 34–42, https://doi.org/10.1016/j.mineng.2016.12.004.

[3] Z. Bian, X. Miao, S. Lei, S. Chen, W. Wang, S. Struthers, The challenges of reusing mining and mineral-processing wastes, Science 337 (2012) 702–703, https://doi.org/10.1126/science.1224757.

[4] D.M. Franks, M. Stringer, L.A. Torres-Cruz, E. Baker, R. Valenta, K. Thygesen, A. Matthews, J. Howchin, S. Barrie, Tailings facility disclosures reveal stability risks, Sci. Rep. 11 (2021) 5353, https://doi.org/10.1038/s41598-021-84897-0.

[5] Y. Jiao, C. Zhang, P. Su, Y. Tang, Z. Huang, T. Ma, A review of acid mine drainage: Formation mechanism, treatment technology, typical engineering cases and resource utilization, Process Saf. Environ. Prot. 170 (2023) 1240–1260, https://doi.org/10.1016/j.psep.2022.12.083.

[6] M. Azizi, A. Faz, R. Zornoza, S. Martínez-Martínez, V. Shahrokh, J.A. Acosta, Environmental pollution and depth distribution of metal(loid)s and rare earth elements in mine tailing, J. Environ. Chem. Eng. 10 (2022) 107526, https://doi.org/10.1016/j.jece.2022.107526.

[7] European Commission, Study on the Critical Raw Materials for the EU 2023 – Final Report, n.d.

[8] U.S. Geological Survey, Department of Interior, 2022 Final List of Critical Minerals, n.d.

[9] V. Balaram, Rare earth elements: a review of applications, occurrence, exploration, analysis, recycling, and environmental impact, Geosci. Front. 10 (2019) 1285–1303, https://doi.org/10.1016/j.gsf.2018.12.005.

[10] Z.M. Migaszewski, A. Gałuszka, S. Dołęgowska, Extreme enrichment of arsenic and rare earth elements in acid mine drainage: Case study of Wiśniówka mining area (south-central Poland), Environ. Pollut. 244 (2019) 898–906, https://doi.org/10.1016/j.envpol.2018.10.106.

[11] C.R. Cánovas, S. Chapron, G. Arrachart, S. Pellet-Rostaing, Leaching of rare earth elements (REEs) and impurities from phosphogypsum: a preliminary insight for further recovery of critical raw materials, J. Clean. Prod. 219 (2019) 225–235, https://doi.org/10.1016/j.jclepro.2019.02.104.

[12] M. Salo, O. Knauf, J. Mäkinen, X. Yang, P. Koukkari, Integrated acid leaching and biological sulfate reduction of phosphogypsum for REE recovery, Miner. Eng. 155 (2020) 106408, https://doi.org/10.1016/j.mineng.2020.106408.

[13] J.C. Fortes, A.M. Sarmiento, A.T. Luis, M. Santisteban, J.M. Davila, F. Córdoba, J. A. Grande, Wasted critical raw materials: a polluted environmental scenario as potential source of economic interest elements in the Spanish part of the Iberian pyrite belt, Water Air Soil Pollut. 232 (2021) 88, https://doi.org/10.1007/s11270-021-05018-1.

[14] A.J. Goodman, A.J. Bednar, J.F. Ranville, Rare earth element recovery in hard-rock acid mine drainage and mine waste: a case study in Idaho Springs, Colorado, Appl. Geochem. 150 (2023) 105584, https://doi.org/10.1016/j.apgeochem.2023.105584.

[15] T. Chen, C. Lei, B. Yan, X. Xiao, Metal recovery from the copper sulfide tailing with leaching and fractional precipitation technology, Hydrometall. 147–148 (2014) 178–182, https://doi.org/10.1016/j.hydromet.2014.05.018.

[16] B. Zhang, C. Liu, C. Li, M. Jiang, A novel approach for recovery of rare earths and niobium from Bayan Obo tailings, Miner. Eng. 65 (2014) 17–23, https://doi.org/10.1016/j.mineng.2014.04.011.

[17] K. Menzel, L. Barros, A. García, R. Ruby-Figueroa, H. Estay, Metal sulfide precipitation coupled with membrane filtration process for recovering copper from acid mine drainage, Sep. Purif. Technol. 270 (2021) 118721, https://doi.org/10.1016/j.seppur.2021.118721.

[18] B.V. Hassas, M. Rezaee, S.V. Pisupati, Effect of various ligands on the selective precipitation of critical and rare earth elements from acid mine drainage, Chemosphere 280 (2021) 130684, https://doi.org/10.1016/j.chemosphere.2021.130684.

[19] Q. Li, W. Zhang, Process development for recovering critical elements from acid mine drainage, Resour. Conserv. Recycl. 180 (2022) 106214, https://doi.org/10.1016/j.resconrec.2022.106214.

[20] A.B. Botelho Junior, D.B. Dreisinger, D.C.R. Espinosa, A review of nickel, copper, and cobalt recovery by chelating ion exchange resins from mining processes and mining tailings, Min. Metall. Explor. 36 (2019) 199–213, https://doi.org/10.1007/s42461-018-0016-8.

[21] M. Hermassi, M. Granados, C. Valderrama, C. Ayora, J.L. Cortina, Recovery of rare earth elements from acidic mine waters: an unknown secondary resource, Sci. Total Environ. 810 (2022) 152258, https://doi.org/10.1016/j.scitotenv.2021.152258.

[22] R.A. Silva, K. Hawboldt, Y. Zhang, Application of resins with functional groups in the separation of metal ions/species – a review, Miner. Process. Extr. Metall. Rev. 39 (2018) 395–413, https://doi.org/10.1080/08827508.2018.1459619.

[23] F. de Dardel, T.V. Arden, Ion Exchangers, in: Ullmanns Encycl. Ind. Chem., John Wiley & Sons, Ltd, 2008, doi: 10.1002/14356007.a14_393.pub2.

[24] W.C. Wilfong, T. Ji, Y. Duan, F. Shi, Q. Wang, M.L. Gray, Critical review of functionalized silica sorbent strategies for selective extraction of rare earth elements from acid mine drainage, J. Hazard. Mater. 424 (2022) 127625, https://doi.org/10.1016/j.jhazmat.2021.127625.

[25] R. Damiche, S. Chafaa, Synthesis of new bioactive aminophosphonates and study of their antioxidant, anti-inflammatory and antibacterial activities as well the assessment of their toxicological activity, J. Mol. Struct. 1130 (2017) 1009–1017, https://doi.org/10.1016/j.molstruc.2016.10.054.

[26] A. Mucha, P. Kafarski, Ł. Berlicki, Remarkable potential of the α-aminophosphonate/phosphinate structural motif in medicinal chemistry, J. Med. Chem. 54 (2011) 5955–5980, https://doi.org/10.1021/jm200587f.

[27] L. Liu, C. Liu, L. Nie, T. Jiang, J. Hong, X. Zhang, L. Luo, X. Wang, Study on the synergistic antibacterial effect of silver-carried layered zirconium alkyl-N, N-dimethylenephosphonate, Inorganica Chim. Acta 435 (2015) 66–72, https://doi.org/10.1016/j.ica.2015.06.002.

[28] S. Kuang, W. Liao, Progress in the extraction and separation of rare earths and related metals with novel extractants: a review, Sci. China Technol. Sci. 61 (2018) 1319–1328, https://doi.org/10.1007/s11431-018-9295-0.

[29] E.J. Virtanen, S. Perämäki, K. Helttunen, A. Väisänen, J.O. Moilanen, Alkyl-substituted aminobis(phosphonates)—efficient precipitating agents for rare earth elements, thorium, and uranium in aqueous solutions, ACS Omega 6 (2021) 23977–23987, https://doi.org/10.1021/acsomega.1c02982.

[30] M.H. Kudzin, J. Drabowicz, F. Jordan, Z.H. Kudzin, P. Urbaniak, Reactivity of aminophosphonic acids. 2. Stability in solutions of acids and bases, Phosphorus Sulfur Silicon Relat. Elem. 194 (2019) 326–328, https://doi.org/10.1080/10426507.2018.1540002.

[31] S. Virolainen, E. Repo, T. Sainio, Recovering rare earth elements from phosphogypsum using a resin-in-leach process: selection of resin, leaching agent, and eluent, Hydrometall. 189 (2019) 105125, https://doi.org/10.1016/j.hydromet.2019.105125.

[32] R. Thapa, A. Rahmani, P. Turhanen, A. Taskinen, T. Nissinen, R. Neitola, J. Vepsäläinen, V.-P. Lehto, J. Riikonen, Recovery of uranium with bisphosphonate modified mesoporous silicon, Sep. Purif. Technol. 272 (2021) 118913, https://doi.org/10.1016/j.seppur.2021.118913.

[33] M. Hermassi, M. Granados, C. Valderrama, C. Ayora, J.L. Cortina, Recovery of Rare Earth Elements from acidic mine waters by integration of a selective chelating ion-exchanger and a solvent impregnated resin, J. Environ. Chem. Eng. 9 (2021) 105906, https://doi.org/10.1016/j.jece.2021.105906.

[34] M. Hermassi, M. Granados, C. Valderrama, N. Skoglund, C. Ayora, J.L. Cortina, Impact of functional group types in ion exchange resins on rare earth element recovery from treated acid mine waters, J. Clean. Prod. 379 (2022) 134742, https://doi.org/10.1016/j.jclepro.2022.134742.

[35] M.J. Page, K. Soldenhoff, M.D. Ogden, Comparative study of the application of chelating resins for rare earth recovery, Hydrometall. 169 (2017) 275–281, https://doi.org/10.1016/j.hydromet.2017.02.006.

[36] K.L. Ang, D. Li, A.N. Nikoloski, The effectiveness of ion exchange resins in separating uranium and thorium from rare earth elements in acidic aqueous sulfate media. Part 2. Chelating resins, Miner. Eng. 123 (2018) 8–15, https://doi.org/10.1016/j.mineng.2018.04.017.

[37] E. Lahtinen, M.M. Hänninen, K. Kinnunen, H.M. Tuononen, A. Väisänen, K. Rissanen, M. Haukka, Porous 3D printed scavenger filters for selective recovery of precious metals from electronic waste, Adv. Sustain. Syst. 2 (2018) 1800048, https://doi.org/10.1002/adsu.201800048.

[38] K. Ibebunjo, Y. El Ouardi, J. Kwame Bediako, A. Iurchenkova, E. Repo, Functionalization of recycled polymer and 3D printing into porous structures for selective recovery of copper from copper tailings, Chem. Eng. Sci. 286 (2024) 119664, https://doi.org/10.1016/j.ces.2023.119664.

[39] N.P.F. Gonçalves, E.F. da Silva, L.A.C. Tarelho, J.A. Labrincha, R.M. Novais, Simultaneous removal of multiple metal(loid)s and neutralization of acid mine drainage using 3D-printed bauxite-containing geopolymers, J. Hazard. Mater. 462 (2024) 132718, https://doi.org/10.1016/j.jhazmat.2023.132718.

[40] M. Rodas Ceballos, F. González Serra, J.M. Estela, V. Cerdà, L. Ferrer, 3D printed resin-coated device for uranium (VI) extraction, Talanta 196 (2019) 510–514, https://doi.org/10.1016/j.talanta.2018.12.055.

[41] S. Fuxiang, W. Na, Z. Qiangqiang, W. Jie, L. Bin, 3D printing calcium alginate adsorbents for highly efficient recovery of U(VI) in acidic conditions, J. Hazard. Mater. 440 (2022) 129774, https://doi.org/10.1016/j.jhazmat.2022.129774.

[42] C. Calderilla, F. Maya, V. Cerdà, L.O. Leal, 3D printed device including disk-based solid-phase extraction for the automated speciation of iron using the multisyringe flow injection analysis technique, Talanta 175 (2017) 463–469, https://doi.org/10.1016/j.talanta.2017.07.028.

[43] C. Calderilla, F. Maya, V. Cerdà, L.O. Leal, 3D printed device for the automated preconcentration and determination of chromium (VI), Talanta 184 (2018) 15–22, https://doi.org/10.1016/j.talanta.2018.02.065.

[44] O. Halevi, T.-Y. Chen, P. See Lee, S. Magdassi, J.A. Hriljac, Nuclear wastewater decontamination by 3D-Printed hierarchical zeolite monoliths, RSC Adv. 10 (2020) 5766–5776, https://doi.org/10.1039/C9RA09967K.

[45] E. Lahtinen, L. Kivijärvi, R. Tatikonda, A. Väisänen, K. Rissanen, M. Haukka, Selective recovery of gold from electronic waste using 3D-printed scavenger, ACS Omega 2 (2017) 7299–7304, https://doi.org/10.1021/acsomega.7b01215.

[46] M. Haukka, K. Rissanen, A. Väisänen, E. Lahtinen, L. Kivijärvi, A porous body, method for manufacturing it and its use for collecting substance from source material, PCT Pat application No 050533, 2018.

[47] J. Frimodig, M. Haukka, Removal of estrogens from aqueous solutions using 3D-printed polymers, Environ. Sci. Adv. 2 (2023) 1739–1745, https://doi.org/10.1039/D3VA00159H.

[48] S. Dupin, O. Lame, C. Barrès, J.-Y. Charmeau, Microstructural origin of physical and mechanical properties of polyamide 12 processed by laser sintering, Eur. Polym. J. 48 (2012) 1611–1621, https://doi.org/10.1016/j.eurpolymj.2012.06.007.

[49] T. Stichel, T. Frick, T. Laumer, F. Tenner, T. Hausotte, M. Merklein, M. Schmidt, A Round Robin study for selective laser sintering of polymers: back tracing of the

pore morphology to the process parameters, J. Mater. Process. Technol. 252 (2018) 537–545, https://doi.org/10.1016/j.jmatprotec.2017.10.013.
[50] Available at https://github.com/arttumiettinen/pi2, n.d.
[51] N. Otsu, A threshold selection method from gray-level histograms, IEEE Trans. Syst. Man Cybern. 9 (1979) 62–66, https://doi.org/10.1109/TSMC.1979.4310076.
[52] T. Hildebrand, P. Rüegsegger, A new method for the model-independent assessment of thickness in three-dimensional images, J. Microsc. 185 (1997) 67–75, https://doi.org/10.1046/j.1365-2818.1997.1340694.x.
[53] A. Hubau, A.-G. Guezennec, C. Joulian, C. Falagán, D. Dew, K.A. Hudson-Edwards, Bioleaching to reprocess sulfidic polymetallic primary mining residues: determination of metal leaching mechanisms, Hydrometall. 197 (2020) 105484, https://doi.org/10.1016/j.hydromet.2020.105484.
[54] S. Peelman, D. Kooijman, J. Sietsma, Y. Yang, Hydrometallurgical recovery of rare earth elements from mine tailings and WEEE, J. Sustain. Metall. 4 (2018) 367–377, https://doi.org/10.1007/s40831-018-0178-0.
[55] K. Pyrgaki, V. Gemeni, C. Karkalis, N. Koukouzas, P. Koutsovitis, P. Petrounias, Geochemical occurrence of rare earth elements in mining waste and mine water: a review, Minerals 11 (2021) 860, https://doi.org/10.3390/min11080860.
[56] P.H.N. Vo, S. Danaee, H.T.N. Hai, L.N. Huy, T.A.H. Nguyen, H.T.M. Nguyen, U. Kuzhiumparambil, M. Kim, L.D. Nghiem, P.J. Ralph, Biomining for sustainable recovery of rare earth elements from mining waste: a comprehensive review, Sci. Total Environ. 908 (2024) 168210, https://doi.org/10.1016/j.scitotenv.2023.168210.
[57] I. Langmuir, The constitution and fundamental properties of solids and liquids. Part I. Solids, J. Am. Chem. Soc. 38 (1916) 2221–2295, https://doi.org/10.1021/ja02268a002.
[58] H. Freundlich, G. Losev, Über die Adsorption der Farbstoffe durch Kohle und Fasern, Z. Für Phys. Chem. 59U (1907) 284–312, https://doi.org/10.1515/zpch-1907-5916.
[59] K. Moedritzer, R.R. Irani, The direct synthesis of α-aminomethylphosphonic acids. mannich-type reactions with orthophosphorous acid, J. Org. Chem. 31 (1966) 1603–1607, https://doi.org/10.1021/jo01343a067.
[60] E. Lahtinen, E. Kukkonen, V. Kinnunen, M. Lahtinen, K. Kinnunen, S. Suvanto, A. Väisänen, M. Haukka, Gold nanoparticles on 3D-printed filters: from waste to catalysts, ACS Omega 4 (2019) 16891–16898, https://doi.org/10.1021/acsomega.9b02113.
[61] R. Dai, M. Huang, L. Ma, W. Liu, S. He, H. Liu, C. Zhu, Y. Wang, Z. Zhang, A. Sun, Study on crystal structure and phase transitions of polyamide 12 via wide-angle X-ray diffraction with variable temperature, Adv. Compos. Hybrid Mater. 3 (2020) 522–529, https://doi.org/10.1007/s42114-020-00192-y.
[62] B.H. Stuart, Infrared Spectroscopy: Fundamentals and Applications, John Wiley & Sons, Incorporated, Newark, UNITED KINGDOM, 2004, http://ebookcentral.proquest.com/lib/jyvaskyla-ebooks/detail.action?docID=194354 (accessed January 24, 2024).
[63] P. Larkin, Infrared and Raman Spectroscopy: Principles and Spectral Interpretation, Elsevier, San Diego, United States, 2011, http://ebookcentral.proquest.com/lib/jyvaskyla-ebooks/detail.action?docID=692432 (accessed January 24, 2024).
[64] S. Kuang, Z. Zhang, Y. Li, H. Wei, W. Liao, Extraction and separation of heavy rare earths from chloride medium by α-aminophosphonic acid HEHAPP, J. Rare Earths 36 (2018) 304–310, https://doi.org/10.1016/j.jre.2017.09.007.
[65] K. Gholivand, R. Yaghoubi, A. Farrokhi, S. Khoddami, Two new supramolecular metal diphosphonates: synthesis, characterization, crystal structure and inhibiting effects on metallic corrosion, J. Solid State Chem. 243 (2016) 23–30, https://doi.org/10.1016/j.jssc.2016.07.027.
[66] H.N. Po, N.M. Senozan, The Henderson-Hasselbalch equation: its history and limitations, J. Chem. Educ. 78 (2001) 1499, https://doi.org/10.1021/ed078p1499.
[67] R. Thapa, T. Nissinen, P. Turhanen, J. Määttä, J. Vepsäläinen, V.-P. Lehto, J. Riikonen, Bisphosphonate modified mesoporous silicon for scandium adsorption, Microporous Mesoporous Mater. 296 (2020) 109980, https://doi.org/10.1016/j.micromeso.2019.109980.
[68] N.N.N. Mahasti, Y.-J. Shih, Y.-H. Huang, Removal of iron as oxyhydroxide (FeOOH) from aqueous solution by fluidized-bed homogeneous crystallization, J. Taiwan Inst. Chem. Eng. 96 (2019) 496–502, https://doi.org/10.1016/j.jtice.2018.12.022.
[69] K.Y. Foo, B.H. Hameed, Insights into the modeling of adsorption isotherm systems, Chem. Eng. J. 156 (2010) 2–10, https://doi.org/10.1016/j.cej.2009.09.013.
[70] M.M. Rashad, I.E. El-Sayed, A.A. Galhoum, M.M. Abdeen, H.I. Mira, E.A. Elshehy, S. Zhang, X. Lu, J. Xin, E. Guibal, Synthesis of α-aminophosphonate based sorbents – influence of inserted groups (carboxylic vs. amine) on uranyl sorption, Chem. Eng. J. 421 (2021) 127830, https://doi.org/10.1016/j.cej.2020.127830.
[71] S. Giret, Y. Hu, N. Masoumifard, J.-F. Boulanger, F. Estelle Juère, D.L. Kleitz, Selective separation and preconcentration of scandium with mesoporous silica, ACS Appl. Mater. Interfaces 10 (2018) 448–457, https://doi.org/10.1021/acsami.7b13336.
[72] S. Bao, W. Hawker, J. Vaughan, Scandium loading on chelating and solvent impregnated resin from sulfate solution, Solvent Extr. Ion Exch. 36 (2018) 100–113, https://doi.org/10.1080/07366299.2017.1412917.
[73] Y.-R. Lee, K. Yu, S. Ravi, W.-S. Ahn, Selective adsorption of rare earth elements over functionalized Cr-MIL-101, ACS Appl. Mater. Interfaces 10 (2018) 23918–23927, https://doi.org/10.1021/acsami.8b07130.
[74] Z. Liu, M. Rong, Y. Mi, H. Cai, L. Yang, Phosphorylated porous phenolic resin for efficient extraction of low-concentration rare earth elements from tailing wastewater, Sep. Purif. Technol. 346 (2024) 127502, https://doi.org/10.1016/j.seppur.2024.127502.
[75] R. Turse, W.I. Rieman, Kinetics of ion exchange in a chelating resin, J. Phys. Chem. 65 (1961) 1821–1824, https://doi.org/10.1021/j100827a031.
[76] C. Heitner-Wirguin, J. Kendler, Kinetic behaviour of chelating resins with phosphonic functional groups, J. Inorg. Nucl. Chem. 33 (1971) 3119–3129, https://doi.org/10.1016/0022-1902(71)80078-7.
[77] A.A. Zagorodni, Ion Exchange Materials: Properties and Applications, first edition, Elsevier Science, 2006.
[78] K. Vijayaraghavan, T.V.N. Padmesh, K. Palanivelu, M. Velan, Biosorption of nickel (II) ions onto *Sargassum wightii*: application of two-parameter and three-parameter isotherm models, J. Hazard. Mater. 133 (2006) 304–308, https://doi.org/10.1016/j.jhazmat.2005.10.016.
[79] R.D. Shannon, Revised effective ionic radii and systematic studies of interatomic distances in halides and chalcogenides, Acta Crystallogr. A 32 (1976) 751–767, https://doi.org/10.1107/S0567739476001551.
[80] E. Kukkonen, E.J. Virtanen, J.O. Moilanen, α-Aminophosphonates, -phosphinates, and -phosphine oxides as extraction and precipitation agents for rare earth metals, thorium, and uranium: a review, Molecules 27 (2022) 3465, https://doi.org/10.3390/molecules27113465.
[81] J.E. Bollinger, D.M. Roundhill, Complexation of indium(III), gallium(III), iron(III), gadolinium(III), and neodymium(III) ions with amino diphosphonic acids in aqueous solution, Inorg. Chem. 32 (1993) 2821–2826, https://doi.org/10.1021/ic00065a007.
[82] T.S. Khayyun, A.H. Mseer, Comparison of the experimental results with the Langmuir and Freundlich models for copper removal on limestone adsorbent, Appl. Water Sci. 9 (2019) 170, https://doi.org/10.1007/s13201-019-1061-2.
[83] R.R. Golwankar, T.D.I. Curry, C.J. Paranjothi, J.D. Blakemore, Molecular influences on the quantification of Lewis acidity with phosphine oxide probes, Inorg. Chem. 62 (2023) 9765–9780, https://doi.org/10.1021/acs.inorgchem.3c00084.
[84] J.N. Bentley, S.A. Elgadi, J.R. Gaffen, P. Demay-Drouhard, T. Baumgartner, C. B. Caputo, Fluorescent Lewis adducts: a practical guide to relative Lewis acidity, Organometallics 39 (2020) 3645–3655, https://doi.org/10.1021/acs.organomet.0c00389.
[85] J.R. Gaffen, J.N. Bentley, L.C. Torres, C. Chu, T. Baumgartner, C.B. Caputo, A simple and effective method of determining Lewis acidity by using fluorescence, Chem 5 (2019) 1567–1583, https://doi.org/10.1016/j.chempr.2019.03.022.
[86] K. Ohkubo, S.C. Menon, A. Orita, J. Otera, S. Fukuzumi, Quantitative evaluation of Lewis acidity of metal ions with different ligands and counterions in relation to the promoting effects of Lewis acids on electron transfer reduction of oxygen, J. Org. Chem. 68 (2003) 4720–4726, https://doi.org/10.1021/jo034258u.
[87] K.P. Kepp, A quantitative scale of oxophilicity and thiophilicity, Inorg. Chem. 55 (2016) 9461–9470, https://doi.org/10.1021/acs.inorgchem.6b01702.
[88] Q. Zhao, Z. Zhang, Y. Li, X. Bian, W. Liao, Solvent extraction and separation of rare earths from chloride media using α-aminophosphonic acid extractant HEHAMP, Solvent Extr. Ion Exch. 36 (2018) 136–149, https://doi.org/10.1080/07366299.2018.1431079.
[89] Q. He, J. Chen, L. Gan, M. Gao, M. Zan, Y. Xiao, Insight into leaching of rare earth and aluminum from ion adsorption type rare earth ore: adsorption and desorption, J. Rare Earths 41 (2023) 1398–1407, https://doi.org/10.1016/j.jre.2022.08.009.
[90] M. Traore, A. Gong, Y. Wang, L. Qiu, Y. Bai, W. Zhao, Y. Liu, Y. Chen, Y. Liu, H. Wu, S. Li, Y. You, Research progress of rare earth separation methods and technologies, J. Rare Earths 41 (2023) 182–189, https://doi.org/10.1016/j.jre.2022.04.009.
[91] E.A. Imam, A.I. Hashem, X. Lu, A.A. Tolba, M.G. Mahfouz, J. Xin, I.-E.-T. El-Sayed, S.I. Mohamady, A.A.S. Ahmed, A.A. Galhoum, E. Guibal, Nd(III) sorption using aminophosphonate-based sorbents – sorption properties and application to the treatment of REE concentrate, Colloids Surf. Physicochem. Eng. Asp. 685 (2024) 133339, https://doi.org/10.1016/j.colsurfa.2024.133339.
[92] X. Hu, H. Yang, K. Tan, S. Hou, J. Cai, X. Yuan, Q. Lan, J. Cao, S. Yan, Treatment and recovery of iron from acid mine drainage: a pilot-scale study, J. Environ. Chem. Eng. 10 (2022) 106974, https://doi.org/10.1016/j.jece.2021.106974.
[93] C. Fonseka, S. Ryu, Y. Choo, G. Naidu, J. Kandasamy, R. Thiruvenkatachari, L. Foseid, H. Ratnaweera, S. Vigneswaran, Selective recovery of europium from real acid mine drainage by using novel amine based modified SBA15 adsorbent and membrane distillation system, J. Water Process Eng. 56 (2023) 104551, https://doi.org/10.1016/j.jwpe.2023.104551.
[94] L.B. José, A.C.Q. Ladeira, Recovery and separation of rare earth elements from an acid mine drainage-like solution using a strong acid resin, J. Water Process Eng. 41 (2021) 102052, https://doi.org/10.1016/j.jwpe.2021.102052.
[95] L. Bernardo José, G. Cordeiro Silva, A. Cláudia Queiroz Ladeira, Pre-concentration and partial fractionation of rare earth elements by ion exchange, Miner. Eng. 205 (2024) 108477, https://doi.org/10.1016/j.mineng.2023.108477.
[96] Y. Wang, Y. He, A. Gong, L. Qiu, M. Zhang, M. Traore, X. Zhan, Y. Li, Y. Bai, Y. Liu, G. Gao, W. Zhao, Selective recovery of rare earth metals from acid mine drainage by pyrrolidine diglycolamide silica column, J. Environ. Chem. Eng. 11 (2023) 110091, https://doi.org/10.1016/j.jece.2023.110091.